Low Rank and Sparse Decomposition of Ultrasound Color Flow Images for Suppressing Clutter in Real-Time

Md Ashikuzzaman, Clyde Belasso, Md. Golam Kibria, Andreas Bergdahl, Claudine J. Gauthier and Hassan Rivaz

***Abstract*—In this work, a novel technique for real-time clutter rejection in ultrasound Color Flow Imaging (CFI) is proposed. Suppressing undesired clutter signal is important because clutter prohibits an unambiguous view of the vascular network. Although conventional eigen-based filters are potentially efficient in suppressing clutter signal, their performance is highly dependent on proper selection of a clutter to blood boundary which is done manually. Herein, we resolve this limitation by formulating the clutter suppression problem as a foreground-background separation problem to extract the moving blood component. To that end, we adapt the fast Robust Matrix Completion (fRMC) algorithm, and utilize the in-face extended Frank-Wolfe method to minimize the rank of the matrix of ultrasound frames. Our method automates the clutter suppression process, which is critical for clinical use. We name the method RAPID (Robust mAtrix decomPosition for suppressIng clutter in ultrasounD) since the automation step can substantially streamline clutter suppression. The technique is validated with simulation, flow phantom and two sets of *in-vivo* data. RAPID code as well as most of the data in this paper can be downloaded from RAPID.sonography.ai.**

***Index Terms*—Ultrasound color flow imaging, clutter rejection, robust matrix decomposition, real-time clutter suppression, vessel visualization.**

I. Introduction

Delineating the vasculature and measuring blood flow velocity in order to examine the physiological condition of the local tissue has seen a growing interest during the past few years. Visualizing the vascular structure is immensely important because architectural change in the vascular network may indicate tissue and cell damage leading to ischemia [1], diabetes related diseases [2]–[4] and coronary heart disease [5]–[7]. Aneurysms which appear on the ventricular or atrial vessels may lead to fatal heart attacks [8], [9]. An increased size of the aneurysm might be a potential source of uncontrollable bleeding in the circle of Willis of the brain, abdominal aorta and thoracic aorta [10]–[12]. Furthermore, the gradual development of malignant cells from benign tumors is highly affected by angiogenesis, the physiological process of development of new blood vessels from pre-existing ones [13]–[15]. Visualizing and monitoring of such microscopic change in early stages is of immense importance to warrant better treatment outcomes.

Ultrasound Color Flow Imaging (CFI) is an easy-to-use and cost-effective modality that can be used to observe the blood flow direction and velocity across various vascular networks in the body. The color encoded information in this modality can then be analyzed to determine any potential abnormalities in the region of interest (ROI) [16]. However, ultrasound suffers in its ability to produce a clear visual of the ROI. This is due to scattering which is the result of the beam originating from the transducer travelling through clusters of blood cells as well as other neighbouring structures such as vessel walls and surrounding tissues [17]. In addition, clutter signals originating from stationary or slowly moving tissue components and wave reverberations are the biggest hindrances to visualizing microvascular changes. This is due to the fact that backscattered signals from blood and other tissue exhibit similar properties, especially when blood is moving slowly or tissue is moving rapidly [17]–[19]. Since the backscattered signal from the normal tissue is usually 40 to 100 dB stronger than that of blood [17], it dominates the signal component resulting from moving red blood cell speckles [20] which negatively affects the vessel visualization process. Another important fact is that blood and clutter components possess non-overlapping frequency spectra [18].

The backscattered signal from tissue has a lower Doppler shift than that of blood as tissue velocity is usually slower [17]. This led to using high pass filtering as a promising tool for clutter filtering in the early stages of CFI research. Many methods have been developed to optimally reject unexpected clutter signals from the desired blood components [21]–[23]. Clutter suppression techniques based on high pass filtering can be divided into two broad classes: Finite Impulse Response (FIR) filters [24] and Infinite Impulse Response (IIR) filters [20]. Each of the classes has its own advantages and downsides. Despite having a steeper roll-off, IIR filters suffer from longer settling time [18]. In contrast, FIR filters minimize the settling time, but require a higher order to separate clutter component from blood signal. However, FIR and IIR filters share a common problem of having inadequate slow-time samples leading to ineffective classification of data generated from slowly moving soft tissue and blood [19], [25]. In addition, in cases where unexpected tissue movement dominates, high

Md Ashikuzzaman, Clyde Belasso, Md. Golam Kibria and Hassan Rivaz are with the Department of Electrical and Computer Engineering, Concordia University, Montreal, QC, H3G 1M8, Canada. Email: m_ashiku@encs.concordia.ca, clyde.belasso@gmail.com, m_kibri@encs.concordia.ca and hrivaz@ece.concordia.ca

Claudine J. Gauthier is with the Department of Physics, Concordia University, Montreal, QC, H4B 1R6, Canada. Email: claudine.gauthier@concordia.ca

Andreas Bergdahl is with the Department of Health, Kinesiology & Applied Physiology, Concordia University, Montreal, QC, H4B 2A7, Canada. Email: Andreas.Bergdahl@concordia.ca

pass filters fail to adaptively select the filter cut-off frequency based on clutter characteristics [19], [26].

To resolve the issue of proper cut-off selection, several eigen-based filtering methods have been proposed to discriminate clutter and blood [25], [27]–[29]. The underlying assumption prompting the development of eigen-based techniques is that tissue is spatio-temporally more coherent than blood [18]. The principal idea is to discard the eigen subspace representing the clutter component in the slow-time signal [19]. Initially, one-dimensional spatial and temporal information was taken into account to filter out the clutter signal [30], [31]. These one-dimensional approaches fail to distinguish tissue subspace from blood subspace when the speed of blood is low or the tissue motion is faster than normal [18].

To address the aforementioned shortcomings of one-dimensional investigation, a method [18] based on the Singular Value Decomposition (SVD) and Principal Component Analysis (PCA) of a large Casorati matrix [32] consisting of 2D spatial and temporal coherence has been proposed. Along similar lines, recent work proposed processing the power Doppler images obtained from SVD using Non-local mean based framework, morphological filtering and Hessian-based vessel enhancement techniques [33]–[35]. In addition, motion correction of the acquired ultrasound frames has been introduced to improve the sensitivity of power Doppler imaging [36]. The eigen-based filter has been extended to the 3^{rd} dimension in [37]–[39] using the higher order SVD technique [40]. However, determining the threshold value that separates blood from normal tissue is a challenging task in this method. More specifically, it is assumed that the first few eigen-values are associated with clutter, the next few represents blood, while the rest denote noise [37]. The dimensions of clutter and blood are manually chosen to reject clutter and noise [37]. Having no rigid ground to determine the dimension of clutter, this manual approach is prone to inefficient suppression of clutter. Therefore, recent work [41] proposed 5 parametric and 5 non-parametric methods to select the boundary between clutter and blood subspaces.

To address the aforementioned limitations of PCA- and SVD-based techniques, we propose to look at the clutter suppression problem from the viewpoint of decomposing the data matrix into low rank and sparse components in a computationally efficient manner. The decomposition makes use of the Robust Matrix Completion algorithm, where the low rank component represents the steady tissue signal and the sparse component represents the moving blood echo [42]. More specifically, we organize a series of acquired ultrasound RF frames into a data matrix. Since an ultrasound RF frame contains some measure of echo for each of its sample, the data matrix is complete with no missing element. Therefore, the Robust Matrix Completion Algorithm acts like Robust Principal Component Analysis (RPCA) [43], [44]. Comprehensive studies [45]–[48] have been conducted during the last few years to resolve the matrix rank minimization problem. Many of these algorithms [43], [49] have been successful in the field of computer vision to separate the foreground from the background resulting in automatic separation of foreground and background. However, these techniques are computationally very expensive and also have high memory requirement.

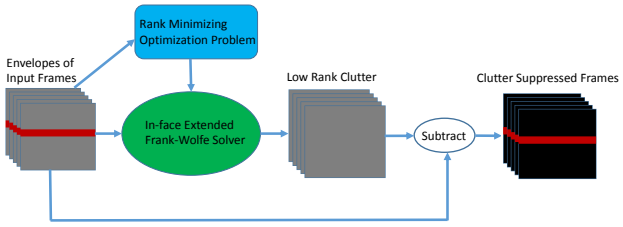

Fig. 1: A flowchart of the proposed RAPID algorithm.

Herein, our goal is to consider blood as the foreground since it is the rapidly moving component, and clutter as the background. Instead of using computationally expensive and memory exhaustive RPCA methods, we have adapted the recently proposed fast Robust Matrix Completion (fRMC algorithm) [50] and the in-face extended Frank-Wolfe method [51] for the purpose of separating the blood component from the stationary tissue echo. As such, we call the algorithm RAPID (**R**obust m**A**trix decom**P**osition for suppress**I**ng clutter in ultrasoun**D**).

RAPID is briefly illustrated in Fig. 1. The main advantage of RAPID is that there is no need to select any threshold manually to separate the blood and clutter components. A shorter version of this work has been presented at the IEEE International Symposium on Biomedical Imaging (IEEE ISBI 2019) [52]. This full version includes more in-depth presentations of the method and results, additional phantom experiments using plane-wave imaging, and two sets of *in-vivo* animal and human subject experiments.

Similar to our previous work [53], we have publicly released the MATLAB code of RAPID, which can be downloaded from RAPID.sonography.ai. The RF data of the phantom experiment and the *in-vivo* rat dataset collected for this work can also be downloaded by following the same link.

II. Experimental Set-up and Data Acquisition

A. Design and Materials for Phantom Experiment

The phantom gel is created from a mixture of water, Knox unflavored gelatin, sugar-free Metamucil psyllium fiber supplement [54], and a container to store the mixture. The venous structure model consisted in an intra-venous (IV) tube passed through a container which has two holes bored on parallel faces of the container. Once the gel mixture is made, it is allowed to congeal and solidify overnight. The solidified gel is then placed in a bain-marie to heat the mixture so that it can liquefy without burning, and is slowly poured into a container with the IV tube, and placed in the refrigerator to solidify.

1) Design and Implementation of the Flow Circuit: The flow circuit is designed to have the fluid of choice flow through the venous structure model at a desired flow rate. The circuit is a closed system, as all the liquids being pumped from the main reservoir returns back to it after having traversed the various channels of the system. The oncoming flow is produced by a siphon pump and controlled by a stopper valve.

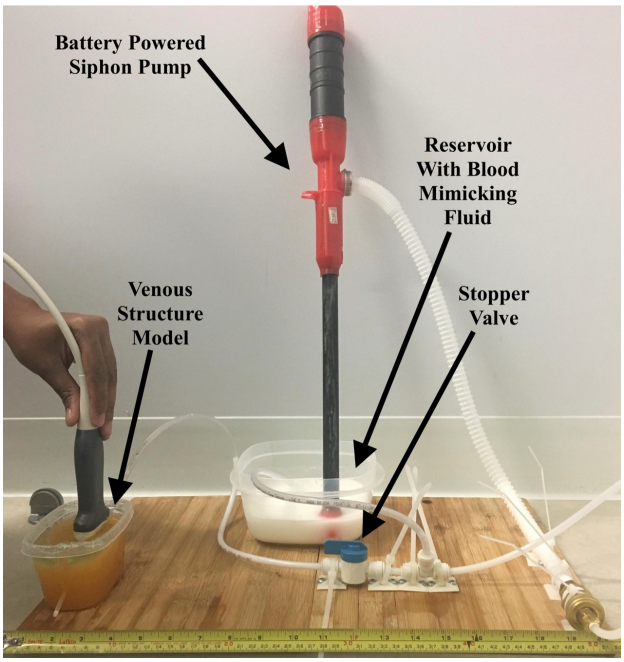

Fig. 2: Data acquisition from the flow phantom with a hand-held L3-12H linear array probe.

For the first two phantom experiments (see Section IV-B), our fluid of choice was water with small amounts of oil and detergent mixed in to create small scatterers. For the third and fourth phantom experiments (see Section IV-B), we used Blood Mimicking Fluid (CIRS: Tissue Simulation & Phantom Technology, Norfolk, VA). Fig. 2 shows the experimental set-up.

B. Simulation of Ultrasound Data

We simulated a tissue with dimensions $3.6\ cm \times 2\ cm \times 1\ cm$ containing a horizontal blood vessel (i.e. perpendicular to the direction of ultrasound wave propagation) of 0.4 cm diameter in the middle using the Field II software package [55], [56]. The flow was laminar with a parabolic velocity profile with the peak velocity of $25\ cms^{-1}$. The frame-rate of ultrasound was set to 1000 fps. The elements of the probe had a width and height of $0.02\ cm$ and $0.5\ cm$ with a kerf of $0.002\ cm$. The sampling frequency was set to $40\ MHz$ whereas the frequency of the probe and fractional bandwidth were $7.27\ MHz$ and 60% respectively, unless otherwise specified. For beamforming, 64 active elements were used.

C. Ultrasound Data Collection

Ultrasound RF data collections were conducted using an Alpinion E-Cube R12 research ultrasound system with an L3-12H linear array probe. In all experiments, the frequency of the probe and the sampling frequency were set to $10\ MHz$ and $40\ MHz$, respectively, unless otherwise specified.

The *in-vivo* experiment on rat was carried out at the Animal Care Facility (ACF) of Concordia University. A 27 week old, Sprague-Dawley male rat was anesthetized before scanning. The rat was placed on a surgery table in supine position as shown in Fig. 3. A portion of the abdominal hair was shaved to prevent large attenuation of waves in the hair. Ultrasound RF data was collected from the abdomen of the rat using the L3-12H linear array probe by conventional focused beamforming. All procedures were approved by the Animal Ethics Committee of Concordia University (#30000259) and were conducted in accordance with guidelines of the Canadian Council on Animal Care.

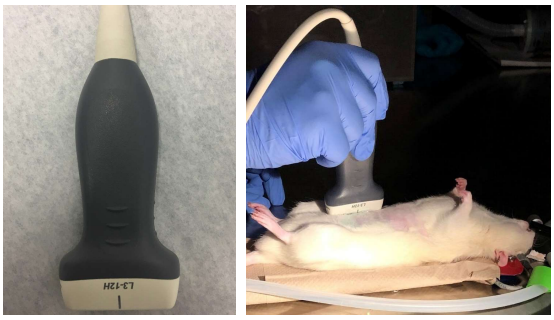

(a) L3-12H Linear Array Probe with Bandwidth = 3 – 12 MHz Footprint = 4.5 cm

(b) *In-vivo* data acquisition from a gas-anesthetized male rat

Fig. 3: Data acquisition from the abdomen of a Sprague-Dawley male rat with a hand-held L3-12H linear array probe. 20 RF frames are collected from one rat.

The human-subject data was collected from the knee of a volunteer using a hand-held probe at Concordia University's PERFORM Centre. The data collection was conducted with an approved ethics from Quebec's Ministere de la Sante et des Services (MSSS).

III. Methods

Assume that we have p ultrasound RF frames of size $m \times n$. The complex envelopes of the RF frames are denoted by $E_i \in \mathbb{C}^{m \times n}$ where $i \in \{1, 2, 3, \ldots, p\}$. All p envelopes are organized in a data matrix $D \in \mathbb{C}^{mn \times p}$ where each column represents the complex envelope of an RF frame. Our purpose is to separate blood and clutter subspaces from the data matrix D. In this section, we first briefly describe the conventional SVD-based algorithm [18], and then elaborate the proposed method.

A. SVD Clutter Suppression

In this method, the data matrix D is decomposed as:

$$D = U\Sigma V^{\dagger} = \sum_{l=1}^{r} \sigma_l u_l v_l^{\dagger} \tag{1}$$

where $U \in \mathbb{C}^{mn \times mn}$ and $V \in \mathbb{C}^{p \times p}$ are unitary matrices containing the left and right singular vectors of D respectively. $\Sigma \in \mathbb{R}^{mn \times p}$ is a diagonal matrix with diagonal entries set to the singular values of D. r = min(mn, p) denotes the rank of the matrix D. σ_l, u_l and v_l stand for singular values and left and right singular vectors of D, respectively. Superscript $\dagger$ denotes the conjugate transpose.

Since mn is usually a very large number, the matrix U cannot be stored in memory of conventional computers (for typical RF signals and $p = 20$ frames, approximately 500 GB of RAM is required to store U). Therefore, only the first $mn \times p$ elements of U are calculated and stored in memory instead of all $mn \times mn$ elements. Similarly for Σ, only the first $p \times p$ elements are calculated and stored in memory. This will lead to a significant reduction in running time and memory requirement. Once the ranks of clutter and blood subspaces c and b are found by manual tuning, the blood subspace is separated from the clutter by:

$$\hat{B} = \sum_{l=c+1}^{c+b} \sigma_l u_l v_l^{\dagger} \tag{2}$$

where $\hat{B}$ represents the blood component of the data matrix. The magnitude of every column of $\hat{B}$ or the power contained in the filtered data can be shown to depict the vasculature.

B. RAPID: Robust Matrix Decomposition in Ultrasound Clutter Suppression

If the correlation coefficient between any two of the p frames is high, the data matrix D can be modelled as a low rank matrix. The blood flow prevents having correlation between entire frames, which can be removed from the data matrix D by solving the following optimization problem [43]:

$$\min\ rank(C) \qquad \text{s.t.} \quad D = C + B$$

where C is the low rank clutter subspace and B denotes the sparse blood component. To solve the optimization problem, we consider the Low Rank Matrix Completion (LRMC) technique where sparsity of the blood component is enforced by solving the following minimization problem:

$$\min\ \|C - D\|_F^2 \qquad \text{s.t.} \quad \|C\|_\star < \delta$$

where $\|.\|_F$ represents the Frobenius norm defined as root sum squared of magnitudes of the matrix entries. $\|.\|_\star$ stands for the nuclear norm of a matrix referring to the sum of its singular values. δ is the radius of the nuclear norm ball of low rank clutter matrix C. Since D is a non-singular matrix and contains envelopes of RF frames in each column, it usually has a large Frobenius norm. Hence the square of the Frobenius norm of D which is defined as the sum of the square of the singular values is greater than the nuclear norm of D. It is mathematically impossible for the nuclear norm of C to be larger than that of D, since C is the underlying low rank component of D. Hence the upper bound of the nuclear norm ball δ can comfortably be set to any value greater or equal to the square of the Frobenius norm of D. In all of our validation examples, we set δ to ten times the square of the Frobenius norm of D. Therefore, RAPID has no tunable parameter.

This is a convex optimization problem [50], [57], which can be efficiently solved by using the recently proposed in-face extended Frank-Wolfe method [51]. It is shown in this work that the low rank structures lie in the boundary of the solution space (Fig. 4), which is exploited to substantially increase the convergence speed and reduce the memory requirements. The algorithm is outlined in Algorithm 1.

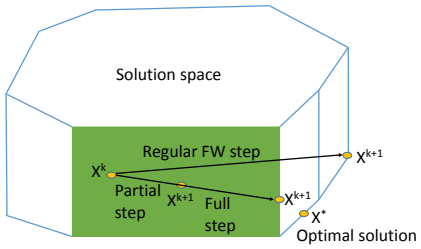

Fig. 4: An illustration of regular and in-face steps of the in-face extended Frank-Wolfe method. Two conditions are checked to decide whether to take the full or partial in-face step. If none of them are satisfied, regular Frank-Wolfe step is chosen.

Algorithm 1: In-face extended Frank-Wolfe algorithm for finding the low-rank clutter subspace

Input : Data matrix D and maximum number of iterations
Output: Optimal low-rank clutter subspace C^*
Definition: C^q is the current iterate of the low rank clutter matrix, $f(C^q) = \frac{1}{2}\|C^q - D\|_F^2$;
while *not converged* **do**
  Calculate $\nabla f(C^q)$: the gradient of $f(C^q)$;
  Compute the direction of next iterate d^q;
  Compute the step size;
  Compute C^{q+1}: check two conditions to determine whether to take full or partial in-face step. If none of the conditions is satisfied, take regular Frank-Wolfe step.
end

The output of this algorithm is the optimal low rank clutter matrix C^*. However, our goal is to find the sparse blood component, which can be obtained by subtracting C^* from D. Every column of B^* $(= D - C^*) \in \mathbb{C}^{mn \times p}$ contains the sparse blood component of individual frames. B^* can be decomposed into p complex frames of size $m \times n$. The magnitude of each of these frames B_i^* can be shown as different images to visualize frame to frame flow. The power Doppler image can be generated with the magnitudes of all p clutter suppressed frames which depicts only the vasculature, not the flow:

$$P(j,k) = \frac{1}{p} \sum_{i=1}^{p} |B_i^*(j,k)|^2 \tag{3}$$

The in-face extended Frank-Wolfe solver offers a substantially faster convergence rate compared to traditional RPCA methods because it does not need to perform SVD in each iteration [51], which leads to significant reductions in its memory footprint and computational complexity. In addition, this solver calculates three directions namely full step, partial step and regular Frank-Wolfe (FW) steps (see the illustration in Fig. 4) for updating the solution in each iteration. A full step is an in-face step suggesting to go to a lower dimensional face. A partial step is also an in-face step which proposes to stay in the relative interior of the current face. If both of the aforesaid directions fail to meet certain criteria [51], the next

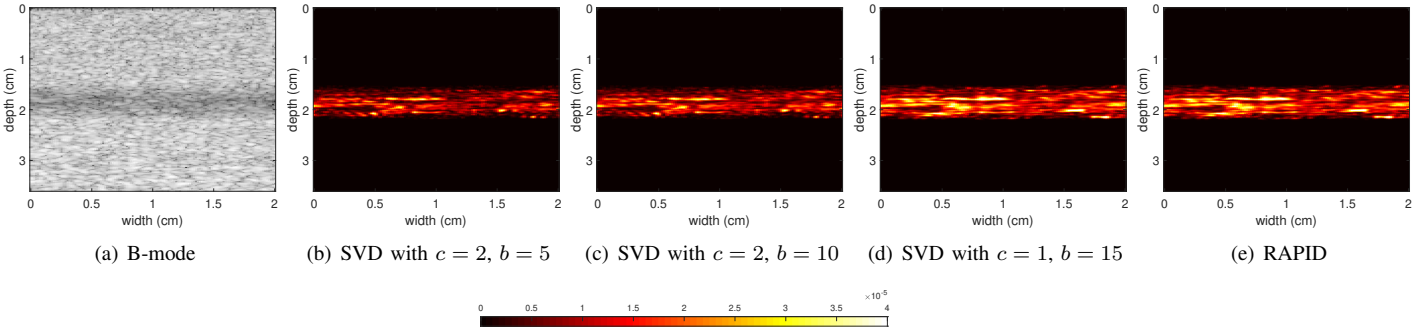

(a) B-mode (b) SVD with $c = 2$, $b = 5$ (c) SVD with $c = 2$, $b = 10$ (d) SVD with $c = 1$, $b = 15$ (e) RAPID

(f) Color bar

Fig. 5: Results of the simulation experiment. Column 1 represents the B-mode image. Columns 2, 3 and 4 depict the power Doppler images from SVD with different combinations of clutter and blood subspace ranks. Column 5 shows the power Doppler image from RAPID. (f) represents the color bar for the power Doppler images.

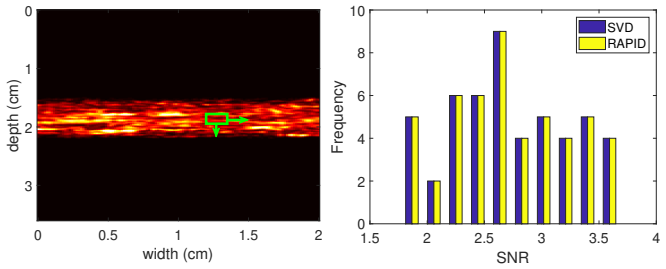

(a) Power Doppler image (b) Histogram of SNR values

Fig. 6: Histogram of SNR values for the simulation experiment. SNR values are calculated on 50 different positions of the moving window shown in the left image.

TABLE I: PSL of the power Doppler images from phantom experiment with conventional imaging. PSL values are calculated on 3 landmarks depicted in Fig. 8(d).

	SVD	RAPID
Landmark 1	40.79	**41.44**
Landmark 2	61.47	**65.01**
Landmark 3	35.16	**36.57**

iterate takes the regular Frank-Wolfe step, which leads to a further reduction of the computational complexity compared to standard RPCA methods.

Effective utilization of thin SVD is a distinctive attribute of in-face extended Frank-Wolfe algorithm. In a certain iteration q, the thin SVD of C^q is updated and stored instead of updating C^q. Given the thin SVD of $C^q = U_q \Sigma_q V_q^\dagger$, the number of entries of U_q, Σ_q and $V_q^\dagger$ are mnr^q, r^q and pr^q respectively, where r^q is the rank of C^q. Therefore, while dealing with the thin SVD instead of the full matrix, only $mnr^q + r^q + pr^q$ number of entries are required to be stored. Since C^q corresponds to a low-rank structure in practice, r^q is small. In such a situation, in-face extended Frank-Wolfe method enables us handle a large data matrix with minimal memory consumption.

TABLE II: PSL of the power Doppler images from phantom experiment with plane-wave imaging. PSL values are calculated on 3 landmarks depicted in Fig. 10(d).

	SVD	RAPID
Landmark 1	54.40	**55.25**
Landmark 2	**49.51**	49.42
Landmark 3	61.30	**61.92**

IV. Results

We validated the proposed RAPID algorithm using simulation, phantom and *in-vivo* experiments. We used $p = 20$ ultrasound frames in all experiments to generate the clutter suppressed image. We compared our results with the conventional SVD-based technique [18]. Along with qualitative comparison of clutter suppressed power Doppler images, we performed quantitative comparison based on Peak-to-Side Level (PSL) and Signal-to-Noise Ratio (SNR), two conventional quality metrics:

$$\text{PSL} = 20\log_{10}\left(\frac{\underline{b}}{\underline{c}}\right), \text{SNR} = \frac{\bar{s}}{\sigma} \tag{4}$$

where $\underline{b}$ and $\underline{c}$ denote the peak intensity at the brightest region of the vessel and intensity at the darkest part of the power Doppler image in neighborhood of the peak respectively. $\bar{s}$ and σ stand for the mean and standard deviation of a spatial window located on the vessel.

The codes of SVD and RAPID were implemented in MATLAB and run on a standard 8^{th} generation $3.2GHz$ Intel core-i7 computer. For SVD, we used the MATLAB command "economy SVD", which only calculates and stores the first p left singular vectors for memory and computational efficiency. The runtime of RAPID is similar to that of economy SVD. Therefore, the proposed method is a potential technique for real-time implementation on commercial ultrasound machines.

A. Simulation Results

Fig. 5 depicts the B-mode image along with the clutter suppressed images for the simulation data. The best result

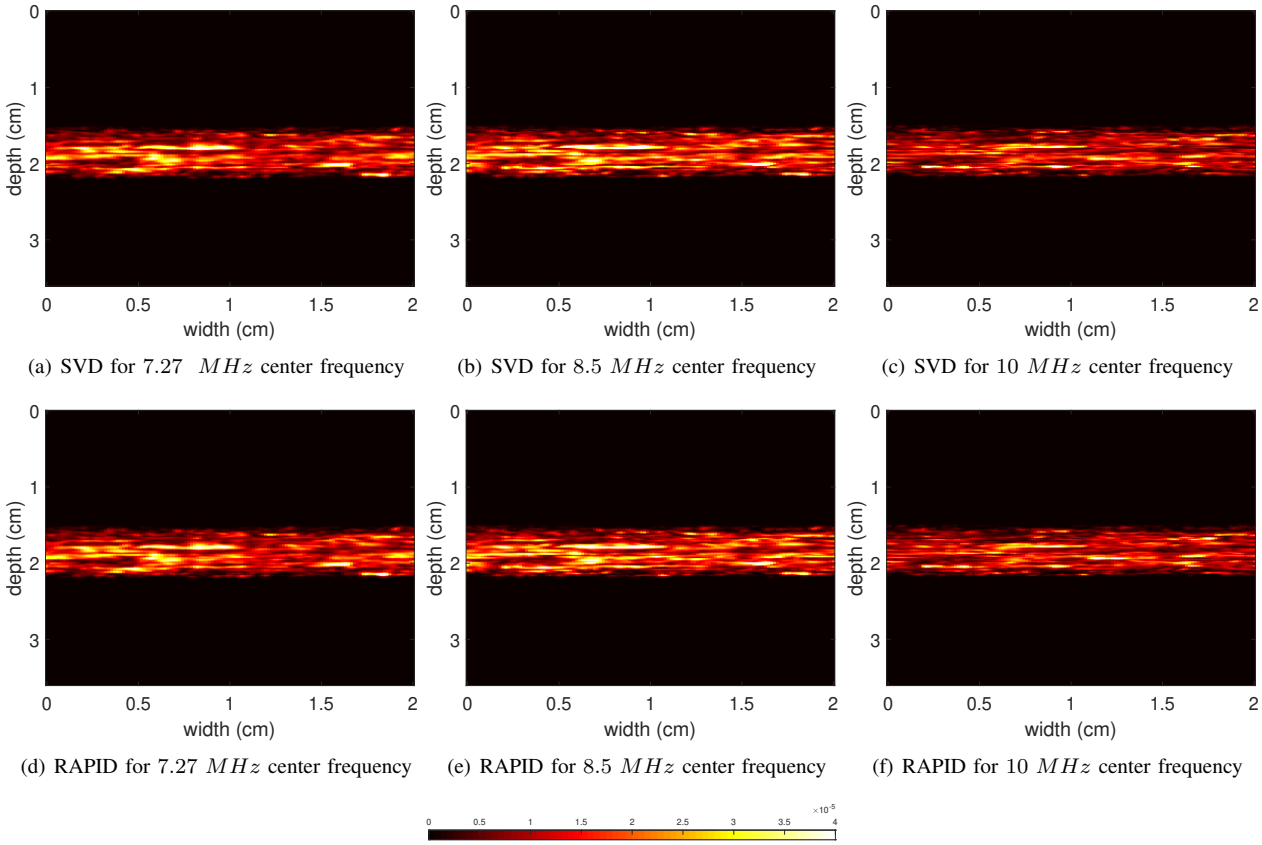

(a) SVD for 7.27 MHz center frequency (b) SVD for 8.5 MHz center frequency (c) SVD for 10 MHz center frequency

(d) RAPID for 7.27 MHz center frequency (e) RAPID for 8.5 MHz center frequency (f) RAPID for 10 MHz center frequency

(g) Color bar

Fig. 7: Results of the simulation experiment for different center frequencies. Columns 1-3 correspond to center frequencies of 7.27 MHz, 8.5 MHz and 10 MHz respectively. Rows 1 and 2 correspond to SVD and RAPID respectively. (g) shows the color bar for the power Doppler images.

from SVD is usually obtained by manually tuning the ranks of clutter and blood subspaces. Power Doppler images generated by SVD with different combinations of clutter and blood ranks are presented in Fig. 5. Visually, the best clutter suppressed image is obtained by setting the clutter and blood ranks to 1 and 15 respectively, as shown in part (d). No manual tuning is necessary for RAPID to obtain the optimal clutter suppressed image. The proposed technique automatically selects the best combinations of ranks. Fig. 5 shows that the result from RAPID is qualitatively similar to the best result obtained by SVD. Since both SVD and RAPID fully suppress the background, we did not calculate PSL to avoid infinite quantitative values [33]. We calculated 50 SNR values for different positions of a moving kernel on the blood vessel. We report the histogram of these 50 SNR values in Fig. 6, which confirms our visual assessment by showing similar SNR values for SVD and RAPID throughout the vessel. The average SNR values corresponding to SVD and RAPID are 2.7174 and 2.7214 respectively. These values are very similar, despite the fact that SVD requires extensive manual intervention to select the boundaries between the subspaces. This, therefore, highlights the quality of our automatic parameter estimation. It is improtant to note that we performed the quantitative comparison between the power Doppler image from RAPID and the best power Doppler image obtained from SVD.

To examine the effect of transmit frequency on clutter rejection, we report the power Doppler images for simulation data collected at three different center frequencies: 7.27 MHz, 8.5 MHz and 10 MHz in Fig. 7. In all three cases, without requiring any parameter tuning, RAPID's performance is similar to the best performance of SVD. The best vessel enhancement is found at a center frequency of 8.5 MHz for both methods. There are two possible reasons. First, since ultrasound images have less resolution at lower frequencies, the clutter suppressed images at 8.5 MHz are better than that at 7.27 MHz. Second, although ultrasound images exhibit higher resolution at lower depths in case of high frequencies, the image quality declines beyond a certain depth due to high attenuation of ultrasound waves. Since our simulation frames contain a vessel at a depth of about 1.8 cm, better performance is achieved at 8.5 MHz compared to 10 MHz. Another reason is that the width of our transducer is equal to λ for the 8.5 MHz center frequency, and therefore, optimal results are obtained with both methods at that frequency.

B. Flow Phantom Results

In the first experiment, conventional focused imaging was performed with a frame rate of 64 fps. Fig. 8 depicts the

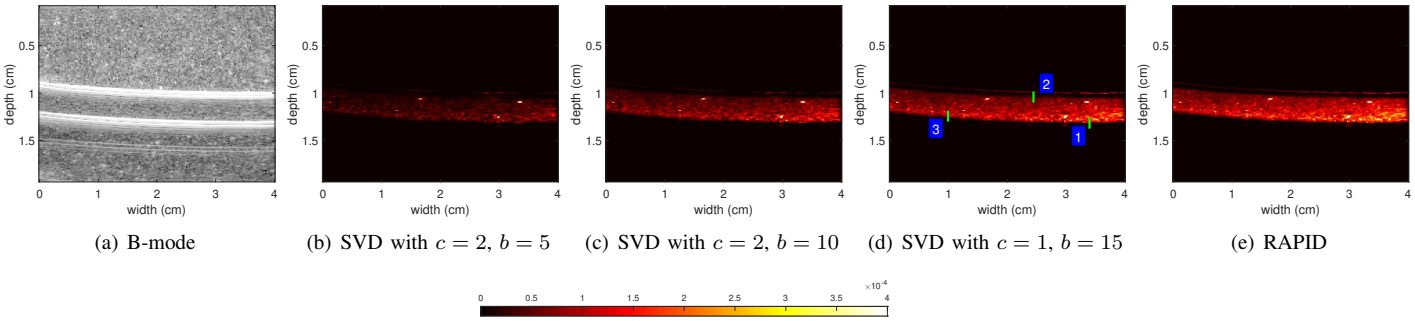

(a) B-mode (b) SVD with $c = 2$, $b = 5$ (c) SVD with $c = 2$, $b = 10$ (d) SVD with $c = 1$, $b = 15$ (e) RAPID

(f) Color bar for conventional data

Fig. 8: Results for the phantom data with focused conventional imaging. Column 1 shows the B-mode image. Columns 2, 3 and 4 represent the power Doppler images from SVD with different combinations of clutter and blood subspace assumptions. Column 5 depicts the power Doppler image from RAPID. (f) represents the color bar for the power Doppler images.

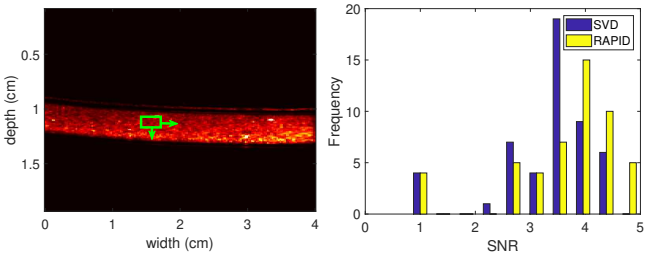

(a) Power Doppler image (b) Histogram of SNR values

Fig. 9: Histogram of SNR values for the phantom data with focused conventional imaging. SNR values are calculated on 50 different positions of the moving window shown in the left image.

clutter rejected images along with the B-mode image. The best result from SVD is selected by manually searching for the best ranks of the clutter and foreground. The result produced by RAPID without requiring any manual tuning (shown in (e)) looks slightly better than the best result from SVD (shown in (d)). Quantitative values of PSL reported in Table I support our visual assessment. PSL values are calculated on three different landmarks of the power Doppler image indicated in Fig. 8(d). In addition, we calculated the SNR at 50 different positions of a moving window (see Fig. 9(a)) on the flow region of the power Doppler image. The SNR values histogram is reported in Fig. 9(b). The histogram shows that RAPID results in a higher frequency in higher SNR values and lower frequency in lower SNR values. Paired *t*-test of the SNR values shows that RAPID statistically outperforms SVD with a p-value of 2.75×10^{-18}. This very low p-value is due to the fact that RAPID outperforms SVD throughout the vessel. Furthermore, SVD and RAPID yield average SNR values of 3.31 and 3.62, respectively showing an improvement of 9.35% by RAPID. It is worth mentioning that quantitative comparison is performed between the result from RAPID and the best result obtained from SVD by manually fine-tuning the boundaries between the subspaces.

In the second experiment, plane-wave data with 11.5 MHz center frequency and a scan rate of 565 fps was collected, with all other imaging parameters the same as the conventional beamforming. Fig. 10 shows the B-mode image, results from SVD for different combinations of clutter and blood ranks and the result from RAPID. Again, RAPID obtains visually superior results compared to SVD by automatically selecting the optimal clutter-blood boundary. We have reported the PSL values calculated on three different landmarks (see Fig. 10(d)) in Table II. These quantitative values also demonstrate that RAPID rejects clutter more efficiently than SVD. In Fig. 11(b), we show the histogram of 50 SNR values calculated at different locations of a moving window (see Fig. 11(a)). The histogram highlights the fact that RAPID results in a higher frequency at higher SNR values. Furthermore, a paired *t*-test shows that RAPID statistically outperforms SVD with a p-value of 6.47×10^{-7}. Averaging of the aforementioned 50 SNR values corresponding to SVD and RAPID resulted in mean values of 2.33 and 2.40, respectively. This implies that RAPID provides a 3.02% improvement in SNR over SVD. Similar to the focused phantom experiment, we have reported the quantitative values for the result from RAPID and the best result from SVD.

In the third experiment, we examined the performance of RAPID and SVD on datasets collected at different center frequencies. We conducted a focused flow phantom experiment where RF frames were acquired at 8.5 MHz and 11.5 MHz transmit frequencies. The B-mode and clutter suppressed images are reported in Fig. 12. In all three cases, RAPID shows similar (if not better) performance as SVD. However, we generate the best results from SVD by extensive manual intervention to select the proper boundaries between subspaces. Best power Doppler images are observed at 11.5 MHz center frequency for both methods. The reason is that the higher frequency image has a good resolution and SNR at shallow depths, where the tube is located.

In the fourth experiment, we investigated the performance of RAPID and SVD with different flow rates by careful mechanical tuning of the flow phantom set-up. We collected RF frames with focused ultrasound imaging from the phantom with flow rates of approximately 1.67 mLs^{-1} (slow flow)

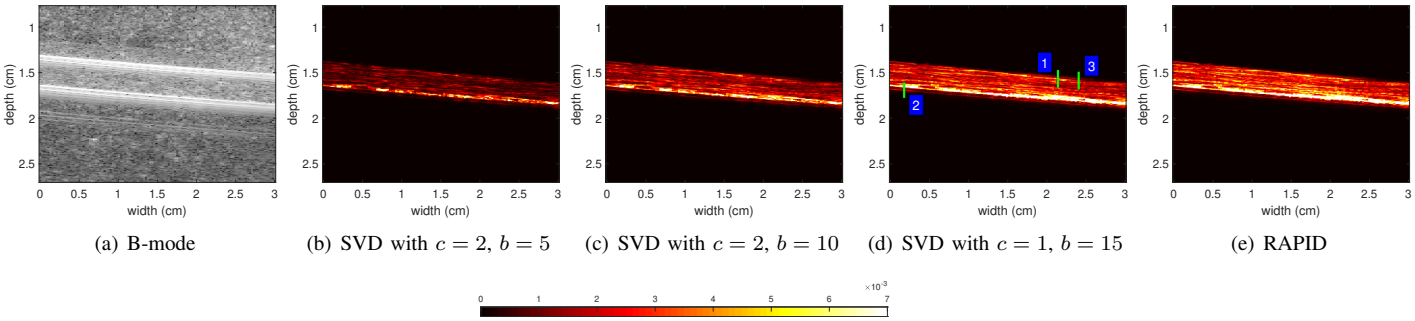

(a) B-mode (b) SVD with $c = 2$, $b = 5$ (c) SVD with $c = 2$, $b = 10$ (d) SVD with $c = 1$, $b = 15$ (e) RAPID

(f) Color bar for plane-wave data

Fig. 10: Results for the phantom data with plane-wave imaging. Column 1 shows the B-mode image. Columns 2, 3 and 4 represent the power Doppler images from SVD with different combinations of clutter and blood subspace assumptions. Column 5 depicts the power Doppler image from RAPID. (f) represents the color bar for the power Doppler images.

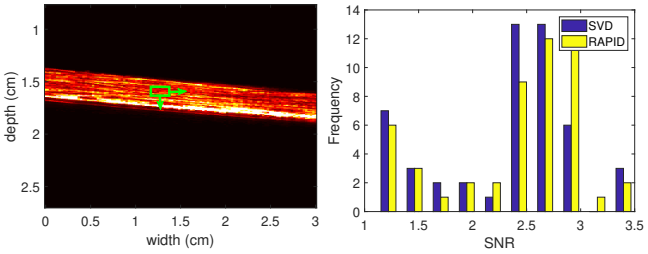

(a) Power Doppler image (b) Histogram of SNR values

Fig. 11: Histogram of SNR values for the phantom data with plane-wave imaging. SNR values are calculated on 50 different positions of the moving window shown in the left image.

and 3.33 mLs^{-1} (fast flow). We show the B-mode and the power Doppler images in Fig. 13. For both flow rates, RAPID performs slightly better than SVD. SVD shows the best power Doppler images when clutter and blood ranks are manually tuned to 1 and 18, respectively. On the other hand, RAPID obtains the optimal power Doppler images automatically. As expected, both SVD and RAPID obtain their best results for the case of fast flow since the difference between tissue clutter and blood becomes dominant at higher flow velocities.

C. *in-vivo* Results

1) Rat Abdomen: B-mode along with the clutter rejected images obtained from SVD and RAPID are reported in Fig. 14. The abdominal aorta and its branches are not clearly visible in the B-mode image, whereas clutter suppressed power Doppler images reveal the vascular structure very well. We show the power Doppler images obtained from SVD for different combinations of ranks associated with clutter and blood subspaces. The best result is obtained assuming clutter and blood ranks as 1 and 15 respectively (in (d)). Visually, the result from RAPID and the best result obtained from SVD are similar. We performed quantitative comparisons between the best power Doppler image obtained from SVD and the power Doppler image generated by RAPID. The PSL values reported in Table III show that SVD and RAPID perform

TABLE III: PSL of the power Doppler images from the *in-vivo* rat experiment. PSL values are calculated on the 3 landmarks depicted in Fig. 14(d).

	SVD	RAPID
Landmark 1	34.27	**34.28**
Landmark 2	**39.86**	39.77
Landmark 3	47.81	**47.86**

almost equally in terms of rejecting clutter. We calculated the PSL values on three landmarks shown in Fig. 14(d). For a more comprehensive investigation, we calculated the SNR values at 50 different locations of a moving window on the vasculature. The histogram of these 50 SNR values reported in Fig. 15 shows that the clutter suppression performance of RAPID is similar to that of SVD. Statistical paired t-test provides a p-value of 0.2226, confirming that there is no significant difference in SNR values of power Doppler images obtained from SVD and RAPID. The average of the 50 SNR values corresponding to SVD and RAPID are 0.9138 and 0.9146, respectively, further highlighting the performance similarity between SVD and RAPID.

2) Human Knee: The conventional beamformed B-mode image as well as the power Doppler images are shown in Fig. 16. It is evident that suppression of clutter aids clear visualization of the lateral inferior genicular artery and branches coming from fibular and anterior recurrent tibial arteries. Fig. 16 also shows that the performance of SVD is highly dependent on the selection of ranks associated with clutter and blood subspaces. In this case, SVD shows its best performance when clutter and blood ranks are considered to be 1 and 15, respectively. In contrast, RAPID is capable of generating the most optimal result without any manual tuning. Visual assessment shows that the power Doppler image obtained from RAPID is similar to the best power Doppler image produced by SVD. Similarly to all other experiments, we compared the result of our method to the best result obtained from SVD quantitatively. PSL values reported in Table IV confirm our visual interpretation. In addition, the histogram of 50 SNR values on different locations of a moving window reported

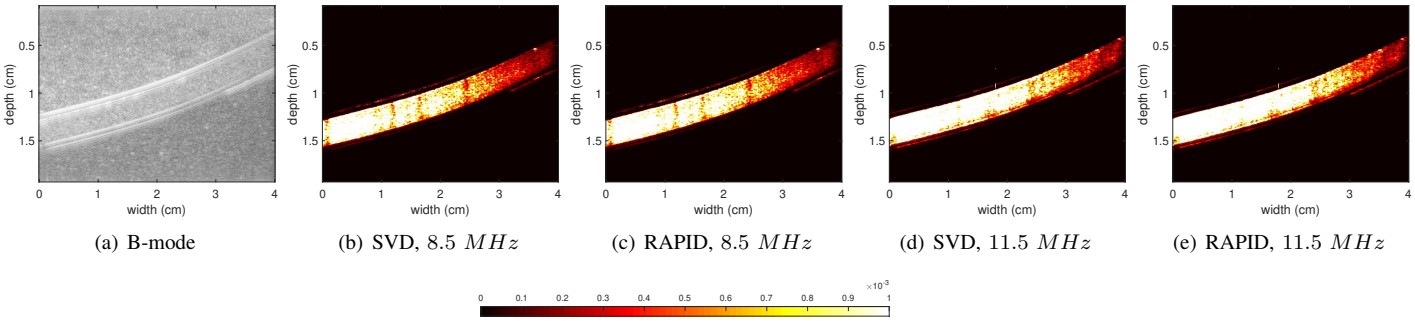

(a) B-mode (b) SVD, 8.5 MHz (c) RAPID, 8.5 MHz (d) SVD, 11.5 MHz (e) RAPID, 11.5 MHz

(f) Color bar

Fig. 12: Results of the conventional flow phantom experiment for different center frequencies. (a) represents the B-mode image. (b) and (c) show power Doppler images obtained by SVD and RAPID, respectively for 8.5 MHz center frequency. (d) and (e) present power Doppler images from SVD and RAPID, respectively for 11.5 MHz center frequency. (f) shows the color bar for the power Doppler images.

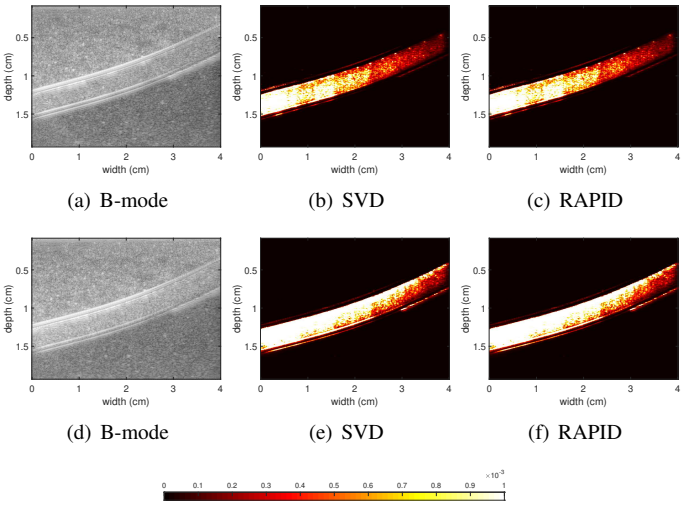

(a) B-mode (b) SVD (c) RAPID

(d) B-mode (e) SVD (f) RAPID

(g) Color bar

Fig. 13: Results of the conventional flow phantom experiment for different flow rates. Columns 1-3 correspond to B-mode, power Doppler images from SVD and RAPID, respectively. Rows 1 and 2 correspond to slow and fast flows, respectively. (g) represents the color bar for the power Doppler images.

TABLE IV: PSL of the power Doppler images from *in-vivo* human knee experiment. PSL values are calculated on the 3 landmarks shown in Fig. 16(d).

	SVD	RAPID
Landmark 1	**60.22**	60.2
Landmark 2	47.02	47.02
Landmark 3	33.77	**33.78**

in Fig. 17 also suggests that SVD and RAPID are similarly effective at suppressing clutter. The average SNR values for SVD and RAPID are 0.9440 and 0.9441, respectively, again showing similar performances.

V. Discussion

It is evident from the results that the clutter suppression efficiency of SVD is highly dependent on proper selection of the ranks of the subspaces, a process that is currently performed manually. This manual involvement hinders clinical adoption of clutter suppression. On the contrary, RAPID selects the ranks automatically with a guarantee of converging to the optimal solution.

SVD is proven to be a promising technique in ultrasound clutter suppression. However, it fails while dealing with data contaminated with outliers [43]. The robustness of RPCA methods to noise is validated with video data in the field of computer vision. Since RF frames acquired with ultrasound are likely to be noisy, robust matrix decomposition methods can potentially be more advantageous than SVD in ultrasound clutter suppression.

The number of frames used to formulate the data matrix is an important concern. Generally, vessels are better visualized when the number of RF frames is increased as more temporal information is incorporated. However, if the data acquisition rate is low, including more frames leads to a significant increase in signal decorrelation noise which might cause the SVD methods to fail. The optimal number of frames likely depends on the imaging frame-rate and extent of physiological motions in tissue. Selection of the optimal number of frames is an interesting avenue of further research.

Here we show that RAPID is capable of obtaining power Doppler images from ultrasound frames collected at different transmit frequencies. However, selection of a proper center frequency is vital for optimally enhancing the vessel. While looking at the superficial vascular structure, a high frequency ultrasound probe should be used for data acquisition to achieve the best resolution. On the other hand, a lower frequency probe is preferable to collect frames from a deeper vascular network, since high frequency ultrasound waves attenuate faster. When we are interested in a vascular structure at moderate depth, careful tuning of transmit frequency is required to compromise between resolution and penetration depth. Another concern is random noise which can be large at deep regions of the

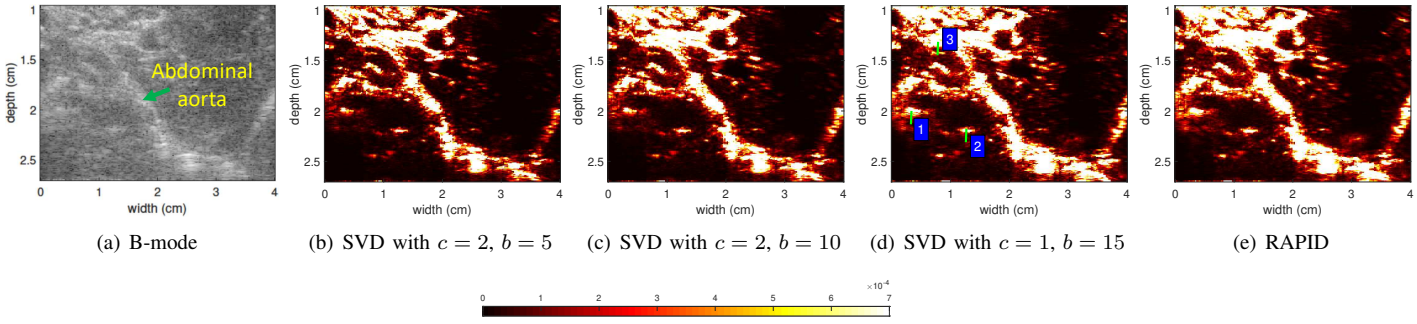

(a) B-mode (b) SVD with $c = 2$, $b = 5$ (c) SVD with $c = 2$, $b = 10$ (d) SVD with $c = 1$, $b = 15$ (e) RAPID

(f) Color bar

Fig. 14: Results obtained from *in-vivo* data collected from the abdomen of a rat. Column 1 depicts the B-mode image. Columns 2, 3 and 4 show the power Doppler images from SVD with different combinations of clutter and blood subspaces. Column 5 presents the power Doppler image from RAPID. (f) shows the color bar for the power Doppler images.

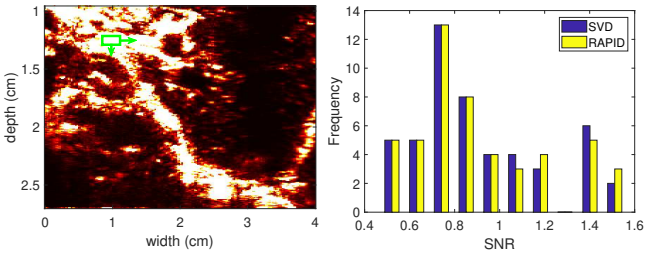

(a) Power Doppler image (b) Histogram of SNR values

Fig. 15: Histogram of SNR values for the *in-vivo* rat experiment. SNR values are calculated at 50 different locations of the moving window shown in the left image.

image for excitations with high center frequencies. Analyzing the performance of RAPID and the validity of the low rank constraint in this situation is an avenue for future work.

In case of slow blood flow, the task of clutter suppression becomes difficult because slowly flowing blood is hardly distinguishable from the steady tissue clutter. However, our investigation on the flow phantom proves that RAPID is capable of generating high quality power Doppler images for both slow and fast flow rates. Although RAPID does not show large improvement over SVD for different flow rates, RAPID converges to the best attainable result without requiring the manual tuning necessary for SVD.

In this work, we conducted the animal experiment with one Sprague-Dawley male rat of age 27 weeks. As our results for simulations, phantom, animal and human experiments are similar, we expect the results to be comparable in more animal experiments. Testing the algorithms in more animal and human experiments is an area of future work.

As the steady background is estimated as a low rank structure in robust matrix decomposition algorithms, high frame to frame correlation is an important requirement. The individual RF frames are stacked in different columns of the data matrix, and as such, should be highly correlated to each other. Therefore, the method could fail in the event of a large out-of-plane movement of the ultrasound probe while collecting the data. Although we did not notice large performance degradation of the proposed RAPID algorithm with possible out-of-plane motion of the probe, 3D data collection from a 2D array can alleviate this problem. Another potential solution to this limitation is introducing a robust image alignment step in every iteration of the RAPID algorithm. The sparsity of the blood component is another important underlying assumption of our algorithm. Although blood is sparser than tissue components in usual scenarios, rapid signal fluctuations caused by turbulent flow in the time domain can affect the spatial sparsity [58]. Imposing the sparsity condition on an appropriate transform (e.g. temporal Fourier Transform) of the blood component instead of the blood component itself might be a promising technique to handle such non-sparsities since the spectral components which lie in the vicinity of the dominant Doppler peak can efficiently represent Doppler shift [58].

VI. Conclusions

In this work, we proposed RAPID: **R**obust m**A**trix de-com**P**osition for suppress**I**ng clutter in ultrasoun**D**, wherein we suggested to enhance blood vessels and suppress unexpected clutter signals by incorporating recently proposed robust matrix completion and optimization algorithms. Validation with simulation, flow phantom and *in-vivo* data proved that RAPID does not require any manual intervention required to select the true boundary between blood subspace and clutter, and as such, automates the process of clutter rejection with a guarantee of optimality. RAPID is also computationally efficient and can be implemented in real-time. These features can potentially help ultrasound-based vascular imaging to reach a wider clinical adoption.

Acknowledgment

This work was supported in part by NSERC Discovery grant RGPIN 2015-04136 and by a New Investigator Award from the Heart and Stroke Foundation.

References

[1] K. Christensen-Jeffries, J. Brown, P. Aljabar, M. Tang, C. Dunsby, and R. J. Eckersley, "3-d in vitroacoustic super-resolution and super-resolved velocity mapping using microbubbles," *IEEE Transactions on Ultrasonics, Ferroelectrics, and Frequency Control*, vol. 64, no. 10, pp. 1478–1486, 2017.

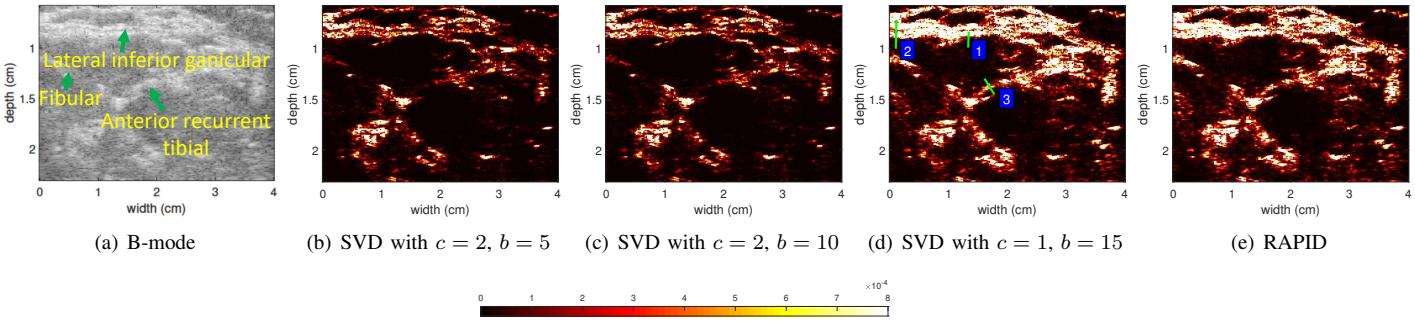

(a) B-mode (b) SVD with $c = 2$, $b = 5$ (c) SVD with $c = 2$, $b = 10$ (d) SVD with $c = 1$, $b = 15$ (e) RAPID

(f) Color bar

Fig. 16: Results obtained from *in-vivo* data collected from the knee of a human subject. Column 1 depicts the B-mode image. Columns 2, 3 and 4 show the power Doppler images from SVD with different combinations of clutter and blood subspaces. Column 5 presents the power Doppler image from RAPID. (f) shows the color bar for the power Doppler images.

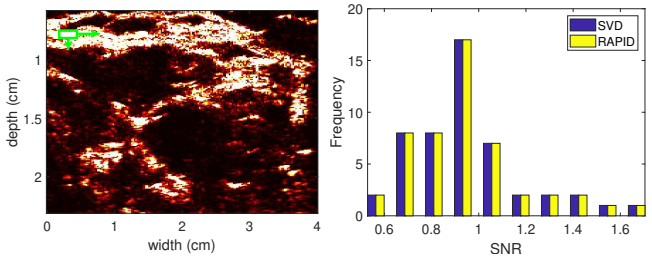

(a) Power Doppler image (b) Histogram of SNR values

Fig. 17: Histogram of SNR values for the *in-vivo* human knee experiment. SNR values are calculated on 50 different locations of the moving window presented in the left image.

[2] A. D. Association, "Peripheral arterial disease in people with diabetes," *Diabetes Care*, vol. 26, no. 12, pp. 3333–3341, 2003.

[3] N. C. Dolan, K. Liu, M. H. Criqui, P. Greenland, J. M. Guralnik, C. Chan, J. R. Schneider, A. L. Mandapat, G. Martin, and M. M. McDermott, "Peripheral artery disease, diabetes, and reduced lower extremity functioning," *Diabetes Care*, vol. 25, no. 1, pp. 113–120, 2002.

[4] R. Zatz and B. M. Brenner, "Pathogenesis of diabetic microangiopathy. the hemodynamic view," *Am. J. Med.*, vol. 80, no. 3, pp. 443–453, 1986.

[5] P. G. Camici and F. Crea, "Coronary microvascular dysfunction," *New Eng. J. Med.*, vol. 356, no. 8, pp. 830–840, 2007.

[6] A. Alrifai, M. Kabach, J. Nieves, J. Pino, and R. Chait, "Microvascular coronary artery disease: Review article," *US Cardiology Review*, vol. 12, no. 1, pp. 41–45, 2018.

[7] M. A. Marinescu, A. I. Lffler, M. Ouellette, L. Smith, C. M. Kramer, and J. M. Bourque, "Coronary microvascular dysfunction, microvascular angina, and treatment strategies," *JACC: Cardiovascular Imaging*, vol. 8, no. 2, pp. 210 – 220, 2015.

[8] G. Zoffoli, D. Mangino, A. Venturini, A. Terrini, A. Asta, C. Zanchettin, and E. Polesel, "Diagnosing left ventricular aneurysm from pseudo-aneurysm: a case report and a review in literature," *J Cardiothorac Surg.*, vol. 4, no. 11, 2009.

[9] S. C. Uppu, R. Sachdeva, and M. Imamura, "Idiopathic giant right atrial aneurysm," *Ann Pediatr Cardiol*, vol. 6, no. 1, pp. 68 – 70, 2013.

[10] J. Cronenwett, T. F Murphy, G. B Zelenock, W. Whitehouse, S. M Lindenauer, L. M Graham, L. E Quint, T. M Silver, and J. Caridi, "Actuarial analysis of variables associated with rupture of small abdominal aortic aneurysms," *Surgery*, vol. 98, no. 3, pp. 472 – 483, 1985.

[11] S. Juvela, M. Porras, and K. Poussa, "Natural history of unruptured intracranial aneurysms: probability of and risk factors for aneurysm rupture," *J. Neurosurgery*, vol. 108, no. 5, pp. 1052 – 1060, 2008.

[12] S. Currie, K. Mankad, and A. Goddard, "Endovascular treatment of intracranial aneurysms: review of current practice," *Postgrad Med J*, vol. 87, no. 1023, pp. 41 – 50, 2011.

[13] K. Christensen-Jeffries, R. J. Browning, M.-X. Tang, C. Dunsby, and R. J. Eckersley, "In vivo acoustic super-resolution and super-resolved velocity mapping using microbubbles," *IEEE Transactions on Medical Imaging*, vol. 34, no. 2, pp. 433–440, 2015.

[14] P. Carmeliet and R. K. Jain, "Angiogenesis in cancer and other diseases," *Nature*, vol. 407, no. 6801, pp. 249 – 257, 2000.

[15] N. Nishida, H. Yano, T. Nishida, T. Kamura, and M. Kojiro, "Angiogenesis in cancer," *Vascular Health and Risk Management*, vol. 2, no. 3, pp. 213 – 219, 2006.

[16] C. R. Merritt, "Doppler color flow imaging," *Journal of Clinical Ultrasound*, vol. 15, no. 9, pp. 591–597, 1987.

[17] S. Bjaerum, H. Torp, and K. Kristoffersen, "Clutter filter design for ultrasound color flow imaging," *IEEE Transactions on Ultrasonics, Ferroelectrics, and Frequency Control*, vol. 49, no. 2, pp. 204–216, 2002.

[18] C. Demen, T. Deffieux, M. Pernot, B. Osmanski, V. Biran, J. Gennisson, L. Sieu, A. Bergel, S. Franqui, J. Correas, I. Cohen, O. Baud, and M. Tanter, "Spatiotemporal clutter filtering of ultrafast ultrasound data highly increases doppler and fultrasound sensitivity," *IEEE Transactions on Medical Imaging*, vol. 34, no. 11, pp. 2271–2285, 2015.

[19] A. C. H. Yu and L. Lovstakken, "Eigen-based clutter filter design for ultrasound color flow imaging: A review," *IEEE Transactions on Ultrasonics, Ferroelectrics, and Frequency Control*, vol. 57, no. 5, pp. 1096–1111, 2010.

[20] A. P. Kadi and T. Loupas, "On the performance of regression and step-initialized iir clutter filters for color doppler systems in diagnostic medical ultrasound," *IEEE Transactions on Ultrasonics, Ferroelectrics, and Frequency Control*, vol. 42, no. 5, pp. 927–937, 1995.

[21] C. Tysoe and D. H. Evans, "Bias in mean frequency estimation of doppler signals due to wall clutter filters," *Ultrasound in Med. & Biol.*, vol. 21, no. 5, pp. 671–677, 1995.

[22] Y. M. Yoo, R. Managuli, and Y. Kim, "Adaptive clutter filtering for ultrasound color flow imaging," *Ultrasound in Med. & Biol.*, vol. 29, no. 9, pp. 1311–1320, 2003.

[23] A. P. G. Hoeks, J. J. W. van de Vorst, A. Dabekaussen, P. J. Brands, and R. S. Reneman, "An efficient algorithm to remove low frequency doppler signals in digital doppler systems," *Ultrasonic Imaging*, vol. 13, pp. 135–144, 1991.

[24] J. A. Jensen, "Stationary echo cancelling in velocity estimation by time-domain cross-correlation," *IEEE Transactions on Medical Imaging*, vol. 12, no. 3, pp. 471–477, 1993.

[25] S. Bjaerum, H. Torp, and K. Kristoffersen, "Clutter filters adapted to tissue motion in ultrasound color flow imaging," *IEEE Transactions on Ultrasonics, Ferroelectrics, and Frequency Control*, vol. 49, no. 6, pp. 693–704, 2002.

[26] A. J. Y. Chee and A. C. H. Yu, "Receiver-operating characteristic analysis of eigen-based clutter filters for ultrasound color flow imaging," *IEEE Transactions on Ultrasonics, Ferroelectrics, and Frequency Control*, vol. 65, no. 3, pp. 390–399, 2018.

[27] M. E. Allam, R. R. Kinnick, and J. F. Greenleaf, "Isomorphism between pulsed-wave doppler ultrasound and direction-of-arrival estimation. ii. experimental results," *IEEE Transactions on Ultrasonics, Ferroelectrics, and Frequency Control*, vol. 43, no. 5, pp. 923–935, 1996.

[28] P. J. Vaitkus, R. S. C. Cobbold, and K. W. Johnston, "A new time-domain narrowband velocity estimation technique for doppler ultrasound flow

imaging. ii. comparative performance assessment," *IEEE Transactions on Ultrasonics, Ferroelectrics, and Frequency Control*, vol. 45, no. 4, pp. 955–971, 1998.

[29] L. A. F. Ledoux, P. Brands, and A. P. G. Hoeks, "Reduction of the clutter component in doppler ultrasound signals based on singular value decomposition: A simulation study," *Ultrasonic imaging*, vol. 19, pp. 1–18, 1997.

[30] J. Bercoff, G. Montaldo, T. Loupas, D. Savery, F. Meziere, M. Fink, and M. Tanter, "Ultrafast compound doppler imaging: providing full blood flow characterization," *IEEE Transactions on Ultrasonics, Ferroelectrics, and Frequency Control*, vol. 58, no. 1, pp. 134–147, 2011.

[31] E. Mace, G. Montaldo, I. Cohen, M. Baulac, M. Fink, and M. Tanter, "Functional ultrasound imaging of the brain," *Nature Methods*, vol. 8, pp. 662–664, 2011.

[32] E. J. Candes, C. A. Sing-Long, and J. D. Trzasko, "Unbiased risk estimates for singular value thresholding and spectral estimators," *IEEE Transactions on Signal Processing*, vol. 61, no. 19, pp. 4643–4657, 2013.

[33] M. Bayat, M. Fatemi, and A. Alizad, "Background removal and vessel filtering of noncontrast ultrasound images of microvasculature," *IEEE Transactions on Biomedical Engineering*, vol. 66, no. 3, pp. 831–842, 2019.

[34] S. Adabi, S. Ghavami, M. Fatemi, and A. Alizad, "Non-local based denoising framework for in vivo contrast-free ultrasound microvessel imaging," *Sensors*, vol. 19, 2019.

[35] I. zdemir and K. Hoyt, "Morphological processing for multiscale analysis of super-resolution ultrasound images of tissue microvascular networks," in *SPIE Medical Imaging*, 2019.

[36] R. Nayak, V. Kumar, J. Webb, A. Gregory, M. Fatemi, and A. Alizad, "Non-contrast agent based small vessel imaging of human thyroid using motion corrected power doppler imaging," *Scientific Reports*, vol. 8, 2018.

[37] M. Kim, C. K. Abbey, J. Hedhli, L. W. Dobrucki, and M. F. Insana, "Expanding acquisition and clutter filter dimensions for improved perfusion sensitivity," *IEEE Transactions on Ultrasonics, Ferroelectrics, and Frequency Control*, vol. 64, no. 10, pp. 1429–1438, 2017.

[38] M. Kim, Y. Zhu, J. Hedhli, L. W. Dobrucki, and M. F. Insana, "Multidimensional clutter filter optimization for ultrasonic perfusion imaging," *IEEE Transactions on Ultrasonics, Ferroelectrics, and Frequency Control*, vol. 65, no. 11, pp. 2020–2029, 2018.

[39] G. G. Olleros, M. B. Stuart, J. A. Jensen, C. A. Villagmez Hoyos, and K. L. Hansen, "Spatiotemporal filtering for synthetic aperture slow flow imaging," in *IEEE IUS*, 2018, pp. 1–4.

[40] G. Bergqvist and E. G. Larsson, "The higher-order singular value decomposition: Theory and an application [lecture notes]," *IEEE Signal Processing Magazine*, vol. 27, no. 3, pp. 151–154, 2010.

[41] J. Baranger, B. Arnal, F. Perren, O. Baud, M. Tanter, and C. Demen, "Adaptive spatiotemporal svd clutter filtering for ultrafast doppler imaging using similarity of spatial singular vectors," *IEEE Transactions on Medical Imaging*, vol. 37, no. 7, pp. 1574–1586, 2018.

[42] Y. Du, M. Zhang, A. C. H. Yu, and W. Yu, "Low-rank adaptive clutter filtering for robust ultrasound vector flow imaging," in *IEEE International Ultrasonics Symposium (IUS)*, 2018, pp. 1–9.

[43] E. J. Candes, X. Li, Y. Ma, and J. Wright, "Robust principal component analysis?" *Journal of the ACM*, vol. 58, no. 3, 2011.

[44] J.-F. Cai, E. J. Candes, and Z. Shen, "A singular value thresholding algorithm for matrix completion," *SIAM J. Optimization*, vol. 20, no. 4, 2010.

[45] V. Chandrasekaran, S. Sanghavi, P. A. Parrilo, and A. S. Willsky, "Rank-sparsity incoherence for matrix decomposition," *SIAM J. Optim.*, vol. 21, no. 2, pp. 572–596, 2011.

[46] J. Wright and Y. Ma, "Dense error correction via ℓ^1-minimization," *IEEE Trans. Information Theory*, vol. 56, no. 7, pp. 3540–3560, 2010.

[47] H. Zhang, W. He, L. Zhang, H. Shen, and Q. Yuan, "Hyperspectral image restoration using low-rank matrix recovery," *IEEE Transactions on Geoscience and Remote Sensing*, vol. 52, no. 8, pp. 4729–4743, 2014.

[48] P. Favaro, R. Vidal, and A. Ravichandran, "A closed form solution to robust subspace estimation and clustering," in *CVPR 2011*, 2011, pp. 1801–1807.

[49] H. Mansour and A. Vetro, "Video background subtraction using semi-supervised robust matrix completion," in *2014 IEEE International Conference on Acoustics, Speech and Signal Processing (ICASSP)*, 2014, pp. 6528–6532.

[50] B. Rezaei and S. Ostadabbas, "Background subtraction via fast robust matrix completion," in *Proceedings of the IEEE International Conference on Computer Vision*, 2017, pp. 1871–1879.

[51] P. G. Robert M. Freund and R. Mazumder, "An extended frank-wolfe method with in-face directions, and its application to low-rank matrix completion," *SIAM J. Optimization*, vol. 27, no. 1, p. 319346, 2017.

[52] M. Ashikuzzaman, C. Belasso, C. J. Gauthier, and H. Rivaz, "Suppressing clutter components in ultrasound color flow imaging using robust matrix completion algorithm: Simulation and phantom study," in *IEEE International Symposium on Biomedical Imaging (IEEE ISBI)*, 2019.

[53] M. Ashikuzzaman, C. J. Gauthier, and H. Rivaz, "Global ultrasound elastography in spatial and temporal domains," *IEEE Transactions on Ultrasonics, Ferroelectrics, and Frequency Control*, vol. 66, no. 5, pp. 876–887, 2019.

[54] J. L. Kendall and J. P. Faragher, "Ultrasound-guided central venous access: a homemade phantom for simulation," *Canadian Journal of Emergency Medicine*, vol. 9, no. 5, p. 371373, 2007.

[55] J. Jensen, "Field: A program for simulating ultrasound systems," *Medical and Biological Engineering and Computing*, vol. 34, pp. 351–352, 1996.

[56] J. Jensen and N. B. Svendsen, "Calculation of pressure fields from arbitrarily shaped, apodized, and excited ultrasound transducers," *IEEE Transactions on Ultrasonics, Ferroelectrics, and Frequency Control*, vol. 39, pp. 262–267, 1992.

[57] X. Peng, C. Lu, Z. Yi, and H. Tang, "Connections between nuclear-norm and frobenius-norm-based representations," *IEEE Transactions on Neural Networks and Learning Systems*, vol. 29, no. 1, pp. 218–224, 2018.

[58] M. Bayat and M. Fatemi, "Concurrent clutter and noise suppression via low rank plus sparse optimization for non-contrast ultrasound flow doppler processing in microvasculature," in *IEEE International Conference on Acoustics, Speech and Signal Processing (ICASSP)*, 2018, pp. 1080–1084.